Spatial characterization of debris ejection from the interaction of a tightly focused PW-laser pulse with metal targets

I.-M. Vladisavlevici[1,2], C. Vlachos[3,4,5], J.-L. Dubois[6,3], D. Haddock[7], S. Astbury[7], A. Huerta[1], S. Agarwal[8,9], H. Ahmed[7], Jon Apiñaniz[1], M. Cernaianu[10], M. Gugiu[10], M. Krupka[8,11], R. Lera[1], A. Morabito[1], D. Sangwan[10], D. Ursescu[10], A. Curcio[1,13], N. Fefeu[3], J. A. Pérez-Hernández[1], T. Vacek[3], P. Vicente[1], Nigel Charles Woolsey[12], G. Gatti[1], M. D. Rodríguez-Frías[1,14], J. J. Santos[3], Philip Bradford[3,7], M. Ehret[1,2*]

[1] *Centro de Láseres Pulsados (CLPU), Villamayor, Spain*
[2] *ELI Beamlines Facility, The Extreme Light Infrastructure ERIC, Dolní Břežany, Czech Republic*
[3] *Univ. Bordeaux - CNRS - CEA, Centre Lasers Intenses et Applications (CELIA), UMR 5107, Talence, France*
[4] *Institute of Plasma Physics and Lasers, University Research and Innovation Centre, Hellenic Mediterranean University, Rethymno, Greece*
[5] *CEA, DAM, DIF, Arpajon, France*
[6] *CEA, DAM, CESTA, Le Barp, France*
[7] *Central Laser Facility, Rutherford Appleton Laboratory, Didcot, United Kingdom*
[8] *FZU-Institute of Physics of Czech Academy of Sciences, Prague, Czech Republic*
[9] *Faculty of Mathematics and Physics, Charles University, Prague, Czech Republic*
[10] *Extreme Light Infrastructure (ELI-NP) and Horia Hulubei National Institute for R & D in Physics and Nuclear Engineering (IFIN-HH), Măgurele, Romania*
[11] *Institute of Plasma Physics of Czech Academy of Sciences, Prague, Czech Republic*
[12] *York Plasma Institute, School of Physics, Engineering and Technology, University of York, York, United Kingdom*
[13] *Istituto Nazionale di Fisica Nucleare - Laboratori Nazionali di Frascati, Frascati (Rome), Italy and*
[14] *Universidad de Alcalá, Madrid, España*

(Dated: January 8, 2025)

We present a novel scheme for rapid quantitative analysis of debris generated during experiments with solid targets following relativistic laser-plasma interaction at high-power laser facilities. Results are supported by standard analysis techniques. Experimental data indicates that predictions by available modeling for non-mass-limited targets are reasonable, with debris on the order of hundreds µg-per-shot. We detect for the first time two clearly distinct types of debris emitted from the same interaction. A fraction of the debris is ejected directional, following the target normal (rear- and interaction side). The directional debris ejection towards the interaction side is larger than on the side of the target rear. The second type of debris is characterized by a more spherically uniform ejection, albeit with a small asymmetry that favours ejection towards the target rear side.

Keywords: debris ejection; high power laser; relativistic laser plasma

I. INTRODUCTION

Established high-power Ti:Sa laser systems [1–9] are able to deliver laser pulses up to several PW at a high-repetition-rate of 0.05 Hz to 1 Hz. Focusing them to relativistic intensities allows to create laser driven secondary sources in a wide range from ionizing radiation [10–13] to XUV- and THz-pulses [14–17]. Solid density metal targets are being used to create ion sources [18, 19], flashes of high energetic X-rays [20, 21] and extreme ultraviolet light sources [22]. A high-repetition-rate operation is important for many applications in medicine and fusion science [23, 24], but poses a challenge for system integrity.

Debris management is an important aspect of ultrahigh intensity laser-solid interaction at high-repetition-rate. The amount of ejected mass ranges in the order of hundreds of µg per laser shot [25, 26] and the deposition of the ablated material is observed to deteriorate beamline components [22, 25, 27]. Available detailed characterizations of debris have been limited to non-relativistic laser intensities just above the ionization threshold [22, 28, 29] and high-energy long-pulse lasers [30]. First characterization attempts for relativistic high-power laser interactions show a timeline of small-most debris particles ejected earlier, with a fast ejection speed, and successively larger projectiles with lower velocity [27]. These studies further indicate an asymmetry of the ejection for early times, with more debris being ejected away from the side on which the laser interaction takes place, but lack a characterization of the spatially resolved debris deposition.

This paper presents a characterization of ejected debris with spatial resolution, for the first time, that will allow an evaluation of mitigation strategies to avoid damage and deterioration of beamline components, diagnostics and metrology devices.

The paper is structured as follows: (i) after a brief introduction of the novel methodology that is used to derive spatially resolved measurements from flatbed scans in Sec. II, (ii) we present results from an experimental campaign at a high-power laser in Sec. III that show two distinct types of debris, and (iii) close with discussion and conclusion in Sec. IV and Sec. V, evaluating the amount

* corresponding author: michael.ehret@eli-beams.eu

10.1017/hpl.2025.12

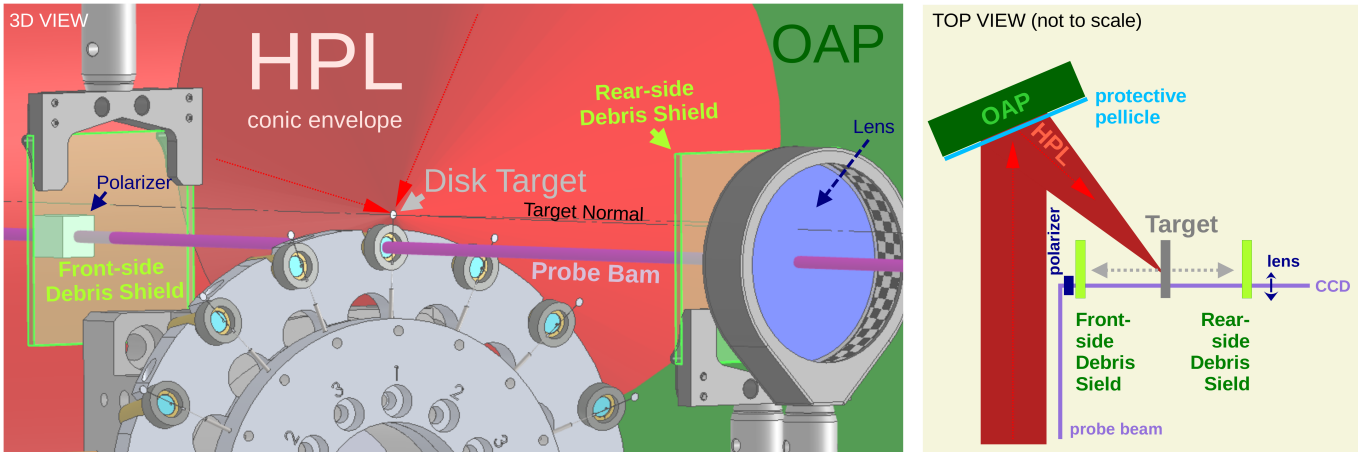

FIG. 1: Two sputter plates from fused silica are used to shield probe beam optics from debris in solid-target experiments at the ELI-NP high-power laser (HPL) facility. Note the laser is focused to relativistic intensities via an off-axis parabola (OAP) onto a disk target, which is protected against debris by a thin pellicle. The front-side debris shield protects a polarizer towards the target normal on the laser-interaction side of a disk target; the rear side debris shield catches debris in front of an imaging lens. The target normal is collinear with the normal of both debris shields.

of ejected debris, relating results to an available model.

II. MATERIALS AND METHODS

Experiments for this work are conducted at the Extreme Light Infrastructure Nuclear Physics (ELI-NP) [31] with a high-power 1 PW Ti:Sa laser delivering on target $E_L \approx 22$ J within a pulse duration of $\tau_L \approx 30$ fs (giving a total power on target of ≈ 0.7 PW). The energy is extrapolated from calibrations recorded at low-energy and the pulse duration is measured on-shot with a FROG system that diagnoses a picked-up reflection from a small elliptical mirror positioned before the focusing parabola. The laser pulse is focused with an incidence angle of 45° onto (50 ± 5) µm thick nickel disk targets, with a focal spot diameter of $d_L \approx 4$ µm full-width at half-maximum (FWHM). The focal spot at high energy is estimated to be the same as for low-energy measurements [32], even if the Strehl ratio might be different [33, 34]. The setup is shown in Fig. 1, with the focusing parabola (OAP) in the back and targets mounted on a wheel.

Two 1 mm thick and 50 mm × 50 mm squared sputter plates from fused silica are used to catch debris that is emitted away from the respective target front and rear sides. The plates were originally meant for another scope, solely to protect the optics of a probe beam setup (not further discussed hereinafter). The front sided sputter plate is placed in front of a polarizer facing the laser-interaction side, while the rear sided sputter plate is placed in front of an imaging lens. Note the auxiliary character of this arrangement of catchers, as the OAP is by default protected with a thin pellicle. The plates' centres are are not perfectly collinear with the laser-interaction point, but shifted by 3 mm down with respect to the target, and their surfaces are parallel to the target surface. The distance of the rear plate to the interaction point is (125 ± 5) mm, the front plate is positioned at (95 ± 10) mm.

After the experiment, the sputter plates are scanned with an EPSON V-750-PRO flatbed scanner to obtain the spatially resolved deposited debris thickness z_{Ni} as a function of the transmittance $T = I_t/I_0$. Here I_0 is the intensity of the incident wave and I_t the intensity at the exit of the double layer system. The details of the scanning procedure are outlined in App. A and the calculation of the transmission of a flat double-layer system is revisited in App. B. The theoretically predicted transmittance of evaporated nickel deposit is shown in Fig. 2 as a function of the layer thickness for three channels of a color scan. One notes the good agreement between the different color channels which points to a flat spectral response.

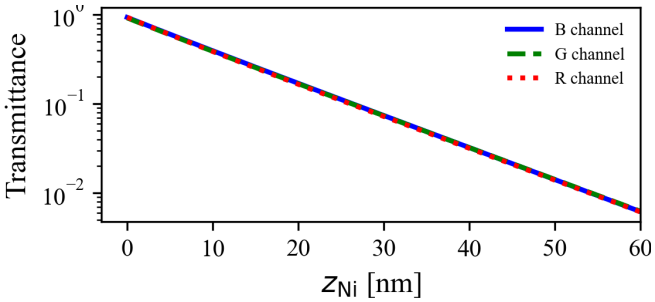

FIG. 2: Predicted transmittance through nickel deposit of thickness z_{Ni} on a 1 mm thick silica plate for three channels of a RGB scan with the EPSON V-750-PRO flatbed scanner.

https://doi.org/10.1017/hpl.2025.12 Published online by Cambridge University Press

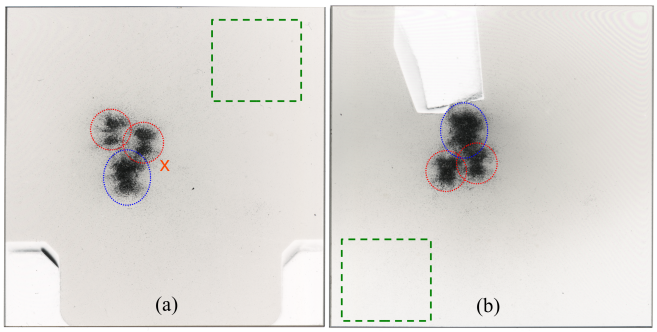

FIG. 3: Debris deposited on silica plates positioned in target normal direction (a) atop the target rear, and (b) atop the target front side facing the high-power laser at ELI-NP 1 PW. Elliptical dashed lines mark areas of a rough surface and the dashed squares indicate ROIs where the debris deposition is uniform. The silica plates are 50 mm squares, visible blank areas stem from mounting clamps used for positioning the plates.

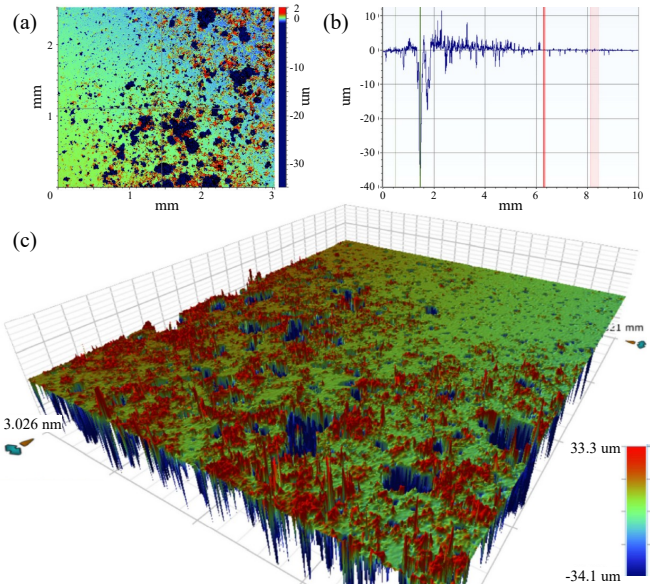

FIG. 4: Detailed view on a mm-scale region in vicinity of rough surface features ("marks") on the lens-sided sputter plate, using (a,c) white-light interferometry, and (b) a profilerometer.

III. RESULTS

Raw scans of debris collected on the sputter plates are shown in Fig. 3, with both plates having recessed areas that were protected from debris by mounting structures. Different interference patterns can be observed in the Fig. 3 (a) and (b), which stem from the slightly different thicknesses of the silica plate. However, their influence on the scanned intensity is smaller than the error bars of the measurements performed. Debris originates from three laser shots, two shots on targets with diameter $d_t = 0.5\,\mathrm{mm}$ and one shot on a disk of 2 mm diameter. The sputter plates are coated by a surfacic deposition of debris, a weak but distinct areal deposition that uniformizes towards the edges of the plates. The uniformity of the deposition can be observed in contrast to the protected area by the sputter plate's holders (white area on Fig. 3).

Additionally, three distinct marks are observed towards the target normal (highlighted with elliptical dashed lines). Slight target misalignment <5° might be responsible for the spatial separation of the marks. This hypothesis is supported by the diametrical opposition of structurally similar marks with respect to the target position. Further, one notes that two small marks (highlighted with red dashed lines) contrast one large mark (highlighted with blue dashed lines) and it is reasonable to assume that small marks correspond to shots on small disk targets. A detailed characterization of the marks is done using White-Light Interferometry, Profilometry and a Scanning Electron Microscope (SEM), shown in Fig. 4 and available as dataset [35]. The surface characteristics change abruptly from uniform deposition outside the marks to a complex ablation-redeposition pattern, likely to be mechanical damage. Ablation craters reach depth of several tens of µm and diameters of hundreds of µm. The average depth is 10 µm (as measured with the profilometer) and the ablated volume within the marks amounts to $\approx 0.0231\,\mathrm{mm}^3$ atop the target front side and $\approx 0.0095\,\mathrm{mm}^3$ atop the target rear side (as deduced from white light interferometry). With a glass density of $5\,\mathrm{g\,cm}^{-3}$, the mass of ablated material from the fused silica plates results to $\approx 115\,\mu\mathrm{g}$ atop the target front side and $\approx 47\,\mu\mathrm{g}$ atop the target rear side. An additional element analysis via Energy Dispersive X-ray Spectroscopy (EDS) in a SEM reveals the atomic composition of the surfacing layer of the sample: $(36.1 \pm 0.4)\,\%$ Ni deposition and $(26.41 \pm 0.50)\,\%$ of Si and O that originate from SiO glass. Further fractions are from contaminations and impurities amounting to $(6.6 \pm 0.6)\,\%$ of O, $(2.2 \pm 0.2)\,\%$ of Cl, and $(2.3 \pm 0.2)\,\%$ of Al. The surfacic deposition of glass indicates the redeposition of ablated material.

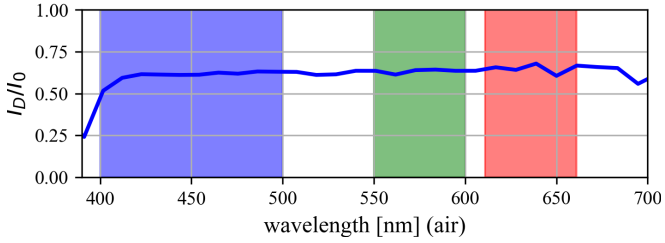

FIG. 5: Spectrally resolved transmittance of nickel debris illuminated with the light source in an EPSON V-750-PRO flatbed scanner; indicated are blue, green and red bands of acquisition for the scanner head. A measurement of intensities I_0 through silica glass is used to normalize the measurement through debris I_D.

https://doi.org/10.1017/hpl.2025.12 Published online by Cambridge University Press

TABLE I: Mean (mea) and maximum (max) transmittance values for the front- and rear side (with respect to the laser interaction) sputter plates across the three color channels of a RGB scan.

		rear side	front side
Blue	mea	$(82.7 \pm 2.6)\,\%$	$(90.8 \pm 3.1)\,\%$
	max	$89.5\,\%$	$96.9\,\%$
Green	mea	$(84.1 \pm 2.9)\,\%$	$(92.2 \pm 3.2)\,\%$
	max	$92.1\,\%$	$98.1\,\%$
Red	mea	$(86.5 \pm 3.1)\,\%$	$(93.2 \pm 3.1)\,\%$
	max	$94.3\,\%$	$99.3\,\%$

TABLE II: Characteristic minimum (min) and mean (mea) thickness values deduced from the transmittance for the front- and rear side sputter plates across the three color channels of a RGB scan.

		rear side	front side
Blue	min	0.42 nm	0.12 nm
	mea	(0.71 ± 0.12) nm	(0.36 ± 0.13) nm
Green	min	0.31 nm	0.07 nm
	mea	(0.65 ± 0.13) nm	(0.31 ± 0.14) nm
Red	min	0.22 nm	0.03 nm
	mea	(0.55 ± 0.14) nm	(0.27 ± 0.13) nm

The transition from regions that show no ablation to regions that are heavily ablated are detailed with color microscopy images in appednix C Fig. 9.

Concerning the surfacic deposition, we measured the transmittance through the centre of the rear side sputter plate (marked with an X point in Fig.3 (a)) with spectral resolution using a compact Czerny-Turner spectrometer, as shown in Fig. 5. The integrated surface element is $1\,\mathrm{mm}^2$. The measurement shows a flat spectral response in accordance with the theoretical prediction presented in Sec. II for the transition metal nickel deposited on a fused silica plate.

The transmittance of the debris in Fig. 3 (a) is shown in Fig. 6 in a squared region-of-interest (ROI) selecting a region of uniform deposition (green squares in Fig. 3) far from the central marks. For conversion from scan intensity to transmittance we follow Eq. A3 from App. A, which reads

$$T_{mn} = 10^{(\ln [I_{mn}]/B)-C} \quad . \tag{1}$$

The raw data is analyzed separately for the distinct RGB channels, revealing no opaque zones which allows for quantitative analysis of the full surface. For all three channels the transmittance shows a similar behaviour, as can be seen in Tab. I. The surfacic deposition on the rear side has a uniform mean transmittance of $(84.4 \pm 2.9)\,\%$ in the ROI. Towards the front side, the mean transmittance amounts to $(92.1 \pm 1.8)\,\%$ in the ROI.

Considering that the debris on the sputter plates consists only of deposited nickel, we calculate the thickness of the deposited debris using Eq. B1 from App. B, which reads

$$T(z_\mathrm{M}, z_\mathrm{S}) = \int_{\omega_-}^{\omega_+} \|\mathfrak{T}(z_\mathrm{M}, z_\mathrm{S}, \omega)\|^2 \cdot s(\omega)\ \mathrm{d}\omega \quad . \tag{2}$$

The results are shown in Fig. 7, and the characteristic values are given in Tab. II. The surfacic deposition on the rear side ROI has a uniform mean thickness of (0.6 ± 0.1) nm. Towards the front side, the mean thickness in the ROI amounts to (0.3 ± 0.1) nm.

The mass can be calculated as $z_\mathrm{Ni} \cdot p^2 \cdot \rho$ with the pixel size $p = 10.6\,\mu\mathrm{m}$ and assuming solid density $\rho = 8.9\,\mathrm{g\,cm^{-3}}$. The total mass of nickel deposited on both plates, within the ROIs from Fig. 6, amounts to 3.3 µg, (2.6 ± 0.8) µg towards the rear side and (1.3 ± 0.4) µg towards the front side. In terms of corresponding debris emission, the average production is $(24 \pm 5)\,\mu\mathrm{g\,sr^{-1}}$ towards the front side and $(83 \pm 15)\,\mu\mathrm{g\,sr^{-1}}$ towards the rear side. Note the non-linear relationship between measured transmittance and derived debris thickness. The emission detected within the surfacic deposition is slightly asymmetric, with larger ejection towards the rear side of the target.

IV. DISCUSSION

Available modelling [26] suggests that shots on small disk targets emit more debris than shots on large disk targets. The prediction for small disks is the total emission of (257 ± 50) µg and (99 ± 20) µg for large disks. This difference between large disks and small disks can be explained by a larger fraction of the laser-heated electrons held back by stronger fields in the case of smaller targets. With a larger refluxing cloud of near-relativistic electrons there are more electrons available to transfer heat to the bulk material. The model applies to cases where the evaporating mass is not limited by the available target mass (here >429 µm diameter disks), and where the target sizes are smaller than the maximum expansion of the laser-generated target potential during electron discharge (here <12 mm disks).

Experimentally, the total mass of the debris can be extrapolated from the measured mean surfacic deposition in the ROIs (towards rear and front side) of $54\,\mu\mathrm{g\,sr^{-1}}$ assuming a spherically uniform emission. The extrapolated result is (672 ± 127) µg and compares well with the modelled total value of (613 ± 83) µg (obtained from the sum of the contribution of two small disks and one large disk) within the margins of uncertainty. The observed small asymmetry of the spherical emission (with more deposition towards the target rear side) might be owed to the asymmetry of the charge distribution in the environment of the laser-interaction, with more electrons deposited in laser forward direction. The asymmetry might be also related to the target thickness, which motivates future

https://doi.org/10.1017/hpl.2025.12 Published online by Cambridge University Press

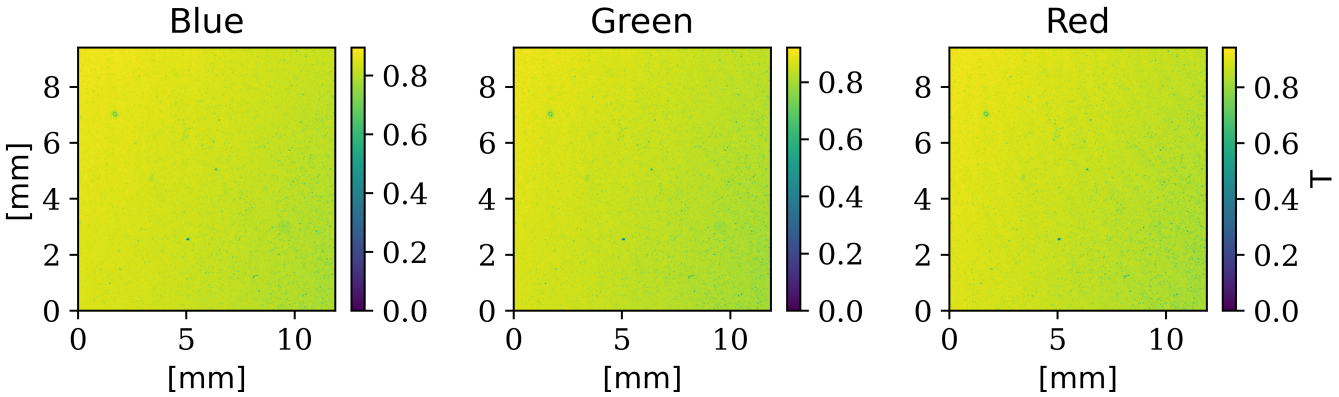

FIG. 6: Transmittance through the debris on the rear side (with respect to the laser interaction) silica plate for all three channels of the RGB scan.

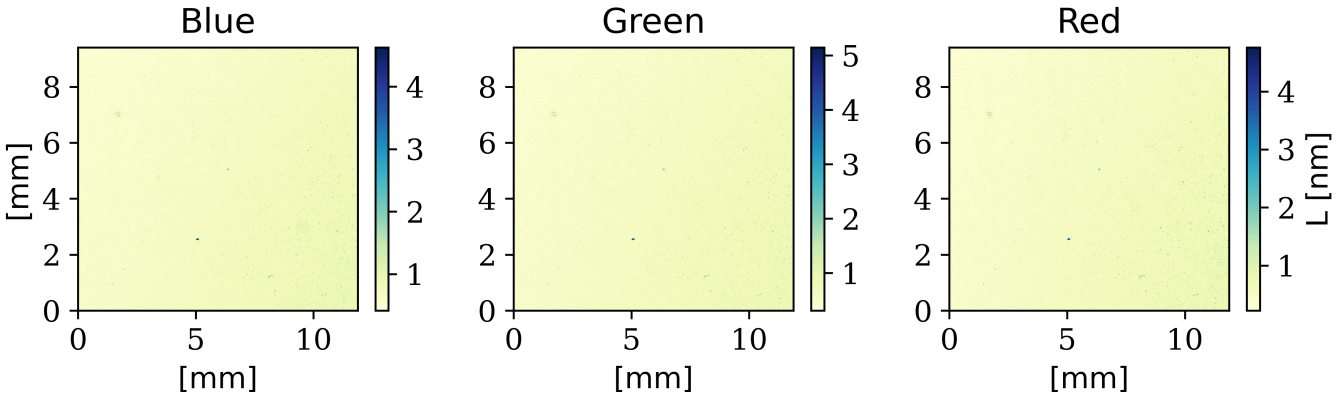

FIG. 7: Thickness of the nickel debris on the rear side silica plate calculated from the transmittance separately for all three channels of the RGB scan.

parametric studies.

The damaged areas on the sputter plates might be produced by the impact of high-velocity debris particles or dense flares of debris. The constraint area of damage reveals this population to be rather directional towards both target normal directions. There is visibly slightly more damage on the sputter plate facing the target front side than towards the target rear side. The amount of ablated glass on the front side is 245 % larger than on the rear side. This might point to the observation of a larger quantity of directional debris towards the target normal on the side of the laser interaction, similar to an earlier observation of this behaviour by N. Booth et al. [27]. This directional emission of destructive debris is favourable in situations of tight laser focusing. The latter is required to reach ultra-high intensities, but brings the precious final focusing optic into close vicinity to the debris source. Directional debris can be mitigated by choosing the laser-incidence angle large enough to avoid an intersection of target normal and focusing optics. The population of debris which is emitted spherically uniform poses a much lower risk as it can be addressed by available mitigation schemes, i.e. spinning protection disks [36].

The experimental results show two small directional marks next to one large mark, which is counter-intuitive when comparing with the modelling that predicts a larger total emission of debris for smaller targets [26]. If the presumption is correct that both small marks correspond to both shots on small targets, then the directional fraction of debris is smaller for small disk targets than for large ones. However, the larger recirculating electron population for smaller targets may yield evaporation to higher temperature, and heating for longer times. Therefore, the amount of spherically emitted debris can be higher for smaller targets than for larger targets. A larger fraction of spherically emitted debris will constraint the directional population.

The characteristic hourglass shape of the directional debris marks might encode valuable information about the laser-target interaction. Studies on laser induced forward and backward transfer in the long-pulse regime show the ejection of debris dependent on laser pulse width, laser pulse energy density and target–catcher distance [37–39]. Further investigation is required to evaluate if debris can be an auxiliary metrology on laser focal spot profile and temporal laser contrast.

This work took benefit of uniform absorption curve

https://doi.org/10.1017/hpl.2025.12 Published online by Cambridge University Press

of nickel across the visible spectrum to introduce a fast spatially resolved way of debris characterization. When using spectrometers instead of a flatbed scanner, surface plasmons might be a way to characterize not only the thickness of a layer but also the size of nano-structures, when using materials that exhibit a large surface plasmon strength [40].

V. CONCLUSION

We present a novel method for the characterization of thin layers of debris deposit based on RGB transmission scans that can be performed with commercial flatbed scanners. Initially transparent debris shields from fused silica are successfully used as debris catchers during experiments with high-power ultra-relativistic laser-pulses irradiating solid density targets. Scans reveal two distinct types of debris: (i) narrow emission cones away from target front- and rear side normal direction, and (ii) spherical emission. While more debris of type (i) is emitted away from the target front, type (ii) shows a slight asymmetry favouring the target rear side. The former agrees with previous works [27], the latter might be due to the overall asymmetric space charge distribution induced by the laser-plasma interaction.

However, the method developed here is applicable only to materials with a smooth transmittance in the optical regime, and cannot be applied to target materials such as semimetals (aluminium) and nobel metals (gold), which exhibit plasmons. Nevertheless, with enough sensor sensitivity, this method can be applied to plastic targets. It is further important for the direct applicability of this method that the surface of the sample is flat, such as the amount of transmitted light is not further reduced by diffuse reflection, which is not taken into account.

The quantitative characterization of the amount of debris and the direction of ejection can be used to promote the implementation of novel schemes that mitigate its deleterious effect on optical components and diagnostics.

AUTHOR CONTRIBUTIONS

The author contributions are as follows: ME commissioned the methodology; CV, AH acquired the data; IMV performed the data curation and analysis; IMV wrote the first draft of the manuscript; JLD, IMV, ME revised the methodology; PWB, ME organized the beamtime at ELI NP; SA, HA, JIA, MC, JLD, MG, MK, RL, DL, AM, DS, DU were involved with underlying experimental work; DH and SA independently performed standard surface analysis; all authors contributed to manuscript improvement, read, and approved the submitted version.

ACKNOWLEDGMENTS

This work would not have been possible without the help of the laser- and the engineering teams at CLPU and ELI NP, and the target fabrication team at CLF. Special thanks for much appreciated support to the workshops of CLPU and ELI NP. The authors are grateful to D. de Luis and to P. Puyuelo Valdés for help in preparing the experimental campaign. This work received funding from the European Union's Horizon 2020 research and innovation program through the European IMPULSE project under grant agreement No. 871161 and LASERLAB-EUROPE V under grant agreement No 871124; from grant PDC2021-120933-I00 funded by MCIN/ AEI / 10.13039/501100011033 and by the European Union NextGenerationEU/PRTR; from grant PID2021-125389OA-I00 funded by MCIN / AEI / 10.13039/501100011033 / FEDER, UE and by "ERDF A way of making Europe", by the European Union and in addition from Unidad de Investigación Consolidada de la Junta de Castilla y León No. CLP087U16. UPM47 campaign was funded through IOSIN, Nucleu PN- IFIN-HH 23-26 Code PN 23 21, and the Extreme Light Infrastructure - Nuclear Physics (ELI-NP) Phase II, a project co-financed by the Romanian Government and the European Union through the European Regional Development Fund and the Competitiveness Operational Programme (1/07.07.2016, COP, ID 1334). This research was funded, in part, by the French Agence Nationale de la Recherche (ANR), Project No. ANR-22-CE30-0044. This research work was also supported by the Ministry of Youth and Sports of the Czech Republic (Project No. LM2023068 and LM2018114 (PALS RI)).

DATA AVAILABILITY STATEMENT

The raw data and numerical methods that support the findings of this study are available from the corresponding author upon reasonable request.

Appendix A: Scanning procedure

Scans with an EPSON V-750-PRO flatbed scanner are performed in both possible orientations (with the debris facing the scanner light source and with the debris facing the scanner readout) and differences are taken into

TABLE III: Grayscale to OD calibration fit parameters for every color channel of an EPSON V-750-PRO.

	B	C
Red	1.333 ± 0.011	8.311 ± 0.067
Green	1.351 ± 0.011	8.199 ± 0.067
Blue	1.471 ± 0.011	7.532 ± 0.067

https://doi.org/10.1017/hpl.2025.12 Published online by Cambridge University Press

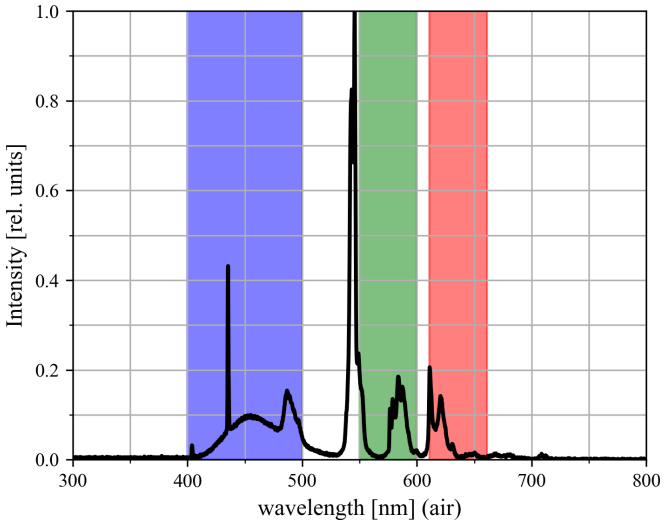

FIG. 8: Normalized spectrum of the light source of the EPSON V-750-PRO flatbed scanner used for this work; with an indication of the blue, green and red bands of acquisition for the scanner head.

account as uncertainty of the intensity ΔI. To improve the estimate of uncertainties of the presented method, RGB-color scans are performed and results of the differing acquisition bands are compared (B : 400 nm to 500 nm; G : 550 nm to 600 nm; R : 611 nm to 661 nm [44]). The spectrum $s(\lambda)$ of the scanner lamp is compared to the acquisition bands in Fig. 8. Here $\lambda = 2\pi c/\omega$ is the vacuum wavelength, with the speed of light c and the frequency of the electromagnetic wave ω.

The transmittance T can be derived from the optical density (OD) of a sample. The OD detected in a pixel of coordinates (m, n) is defined as the logarithmic ratio between the transmitted grayscale intensity $I(m, n)$ and the scanner response for a scan without sample I_0, which can be written as

$$\mathrm{OD} = -\log_{10}\left[\frac{I(m,n)}{I_0}\right] = -\log_{10}\left[T_{mn}\right] \quad . \tag{A1}$$

Kodak WRATTEN 2 Neutral Density No. 96 Filters with well defined spectral properties are used for absolute scanner calibration of transmission scans. The relation of optical density to the transmitted grayscale intensity results to

$$\mathrm{OD} = C - \frac{\ln\left[I_{mn}\right]}{B} \quad , \tag{A2}$$

where B and C are band-dependent fit parameters shown in Tab. III. B represents the inverse scale parameter for the exponential decay and C is the minimum detectable transmittance. The dynamic range on the grayscale can be computed as $\exp\left[B \cdot C\right]$. One retrieves the transmittance as

$$T_{mn} = 10^{(\ln\left[I_{mn}\right]/B) - C} \quad , \tag{A3}$$

with a relative uncertainty of

$$\frac{\Delta T_{mn}}{T_{mn}} = \ln\left[10\right] \cdot \sqrt{\left(\frac{\Delta I_{mn}}{I_{mn} B}\right)^2 + \left(\frac{\ln\left[I_{mn}\right] \Delta B}{B^2}\right)^2 + (\Delta C)^2} \quad . \tag{A4}$$

The relative uncertainty calculates to $\Delta T_{mn}/T_{mn} \approx 16\,\%$ for all color channels on the scale of 16-bit images used for this work, considering a scan-to-scan uncertainty of $\Delta I_{mn}/I_{mn} \approx 1.1\,\%$.

Appendix B: Transmission of a flat double-layer system of debris and catcher

For nm-scale layers of metal deposits on transparent support plates it is possible to retrieve the debris thickness from a measurement of the transmittance

$$T(z_\mathrm{M}, z_\mathrm{S}) = \int_{\omega_-}^{\omega_+} \|\mathfrak{T}(z_\mathrm{M}, z_\mathrm{S}, \omega)\|^2 \cdot s(\omega)\, \mathrm{d}\omega \quad , \tag{B1}$$

where z_M is the thickness of the metal deposit, z_S is the thickness of the support plate, and ω denotes the frequency of the incident electromagnetic waves in a normalized spectrum $\int_{\omega_-}^{\omega_+} s(\omega)\, \mathrm{d}\omega = 1$. In the following equations, the subscript M relates to the metal, and the subscript S relates to the support plate, for all quantities. The transmission ratio $\mathfrak{T}$ for a mono-chromatic incident wave is defined as

$$\mathfrak{T}(z_\mathrm{M}, z_\mathrm{S}, \omega) = E_\mathrm{t}/E_0^+ \tag{B2}$$

with the electric field amplitude of the incident wave E_0^+ and the amplitude at the exit of the double layer system E_t. For normally incident electromagnetic fields, the continuity of electric- and magnetic-field across interfaces between layers of media j and $j+1$ implies at the boundary

$$\begin{aligned} \mathfrak{E}_j^+ + \mathfrak{E}_j^- &= \mathfrak{E}_{j+1}^+ + \mathfrak{E}_{j+1}^- \\ \frac{1}{\eta_j}\left(\mathfrak{E}_j^+ - \mathfrak{E}_j^-\right) &= \frac{1}{\eta_{j+1}}\left(\mathfrak{E}_{j+1}^+ - \mathfrak{E}_{j+1}^-\right) \quad , \end{aligned} \tag{B3}$$

with electric resistance $\eta_j = \sqrt{\mu_j/\epsilon_j}$, where μ_j is the permeability and ϵ_j the permittivity of the respective material. Here the electric field component is described in terms of plane waves $\mathfrak{E}_j^\pm = E_j^\pm \mathrm{e}^{\mp i(z' k_j - \omega t)}$ with wavenumber k_j. Components $\mathfrak{E}_j^+$ are forward propagating (in direction from j to $j+1$) while components $\mathfrak{E}_j^-$ propagate backwards. One obtains

$$\begin{aligned} E_0^+ + E_0^- &= E_\mathrm{M}^+ + E_\mathrm{M}^- \\ \frac{1}{\eta_0}\left(E_0^+ - E_0^-\right) &= \frac{1}{\eta_\mathrm{M}}\left(E_\mathrm{M}^+ - E_\mathrm{M}^-\right) \quad , \end{aligned} \tag{B4}$$

https://doi.org/10.1017/hpl.2025.12 Published online by Cambridge University Press

$$\sum_{p\in\{+1,-1\}} E_{\mathrm{M}}^{p}\mathrm{e}^{-ipz_{\mathrm{M}}k_{\mathrm{M}}} = E_{\mathrm{S}}^{+} + E_{\mathrm{S}}^{-}$$
$$\sum_{p\in\{+1,-1\}} \frac{p}{\eta_{\mathrm{M}}} E_{\mathrm{M}}^{p}\mathrm{e}^{-ipz_{\mathrm{M}}k_{\mathrm{M}}} = \frac{1}{\eta_{\mathrm{S}}}\left(E_{\mathrm{S}}^{+} - E_{\mathrm{S}}^{-}\right) \quad , \tag{B5}$$

$$\sum_{p\in\{+1,-1\}} E_{\mathrm{S}}^{p}\mathrm{e}^{-ipz_{\mathrm{S}}k_{\mathrm{S}}} = E_{\mathrm{t}}$$
$$\sum_{p\in\{+1,-1\}} \frac{p}{\eta_{\mathrm{S}}} E_{\mathrm{S}}^{p}\mathrm{e}^{-ipz_{\mathrm{S}}k_{\mathrm{M}}} = \frac{1}{\eta_0} E_{\mathrm{t}} \quad , \tag{B6}$$

at the entrance (Eqs. B4), middle interface (Eqs. B5) and exit (Eqs. B6) of the double layer system, where E_0^- denotes the reflected wave.

For a first layer of the ferromagnetic transition metal nickel (Ni) followed by a second layer of Fused Silica (FS) one derives

$$\mathfrak{T}(z_{\mathrm{Ni}}, z_{\mathrm{FS}}, \omega) = \frac{8\mathrm{e}^{-iz_{\mathrm{FS}}k_{\mathrm{FS}}}}{m_{+}\mathrm{e}^{iz_{\mathrm{Ni}}k_{\mathrm{Ni}}}\left(n_{+}u_{+} + n_{-}u_{-}\mathrm{e}^{-2iz_{\mathrm{FS}}k_{\mathrm{FS}}}\right) + m_{-}\mathrm{e}^{-iz_{\mathrm{Ni}}k_{\mathrm{Ni}}}\left(n_{-}u_{+} + n_{+}u_{-}\mathrm{e}^{-2iz_{\mathrm{FS}}k_{\mathrm{FS}}}\right)} \tag{B7}$$
$$\| \text{ with } \quad m_{\pm} = 1 \pm n_{\mathrm{Ni}} \tag{B8}$$
$$n_{\pm} = 1 \pm \frac{n_{\mathrm{FS}}}{n_{\mathrm{Ni}}} \tag{B9}$$
$$u_{\pm} = 1 \pm \frac{1}{n_{\mathrm{FS}}} \tag{B10}$$
$$k_j = \frac{n_j\omega}{c} - i\frac{\alpha_j}{2} \tag{B11}$$

where α_j is the absorption coefficient of layer j, and n_j denotes the refractive index respectively. The following approximations of both spectrally resolved quantities are evaluated for wavelengths in the range from 400 nm to 661 nm (from $\omega = 4.71 \times 10^{15}\,\mathrm{s}^{-1}$ to $2.85 \times 10^{15}\,\mathrm{s}^{-1}$ respectively).

The absorption of films of evaporated nickel is [45]

$$\alpha_{\mathrm{Ni}} \approx \left(\frac{\omega}{(1.64 \pm 0.05) \times 10^{18}\,\mathrm{s}^{-1}} + 0.08017\right)\mathrm{nm}^{-1} \quad , \tag{B12}$$

such a monotonic behaviour is common for transition metals that do not build surface plasmons efficiently [46]. Note that the absorption coefficient α_{FS} of silica glass is neglected in the following for its small magnitude [41]. The refractive index of nickel [45] and Fused Silica [42] are

$$n_{\mathrm{Ni}} \approx \frac{(2.43 \pm 0.08) \times 10^{15}\,\mathrm{s}^{-1}}{\omega} + 1.183 \quad , \tag{B13}$$
$$n_{\mathrm{FS}} \approx \left(\frac{\omega}{(3.18 \pm 0.05) \times 10^{16}\,\mathrm{s}^{-1}}\right)^2 + 1.448 \quad . \tag{B14}$$

The evaluation of Eq. B1 can now be performed numerically in spectral slices, i.e. for every color channel of a scan (compare Fig. 8 for the spectrum and the acquisition bands of an EPSON V-750-PRO flatbed scanner). Note that some application cases might be well fitted with an approximated analytical solution for a thin film on a thick finite transparent substrate [43].

Appendix C: Instrumentation for Standard Surface Analysis

1. Elemental analysis

Elemental analysis was performed with Pemtron PS-230AL Scanning Electron Microscope (SEM), fitted with a Bruker QX2 EDX system. It comprises 5-axis motorised stage and tungsten cathode, and a PC controlled compact variable pressure vacuum system.

Method: No gold sample coating was required, as charging was present but not sufficient to affect the EDX spectra. The setup consisted of an electron beam of 20 keV without aperture, a low magnification and low acquisition time of 60 s to avoid over charging. The count rate of X-ray photons detected by the Energy Dispersive X-ray Spectroscopy (EDS) detector for the measurement was 3 kcps.

Results: The atomic percentage of the following materials were found:

https://doi.org/10.1017/hpl.2025.12 Published online by Cambridge University Press

- Nickel 36.14%
- Silicon 26.41%
- Oxygen 32.97%
- Chlorine 2.22%
- Aluminum 2.26%

Note that silicon, oxygen and aluminium are likely present due the glass substrate and SEM chamber background. Both samples (lens and polarizer sputter plates) are considered to have similar results, but this was not explored in detail.

2. 3D area scan

A 3D area scan was performed using the 3D Optical Profilometer Bruker ContourX-100.

Method: The setup consisted of 5x Objective, .55x field of view, 100 µm back scan and forward scan, and a threshold value of 2% (this threshold means that any height variation that is more than 2% of the standard deviation away from the average will be considered significant). This is considered a lenient threshold that would include a lot of noise, but given the sharpness of the features in the sample and the steep wall angles, a higher threshold value excluded too much of the features. Stitching areas were $\sim 15 \times 12$ mm in size consisting of 20+ individual measurements, with a 20% overlap between scans. The area was chosen to include all areas of ablation visible. Data fill was used to approximate missing data in areas of high damage using the software provided data fill algorithm on Vision64 Software.

Results: Data fill was considerable and introduces a lot of uncertainty. The samples are inherently rough and difficult to measure with optical techniques, so no filtering was applied. The depth of ablation areas had poor data acquisition, consequently the step profilometer was considered for more accurate measurements.

3. Surface profile

Surface profile was performed with Dektak Pro Stylus Profilometer. **Method:** The setup consisted of Stylus 2 µm diameter, 10 mm length, Stylus force 10 mg, resolution longitudinal 0.555 µm/pt, resolution quoted as sub 100 nm in height. Data was averaged over 5 scans.

Results: Stylus radius of 2 µm may smooth out the sharpest features. Debris and ablation seem to be immovable and adhered to the substrate such that the probe would not change the substrate during measurement. Multiple measurements were taken and an average of ablation depth was estimated at 10 µm.

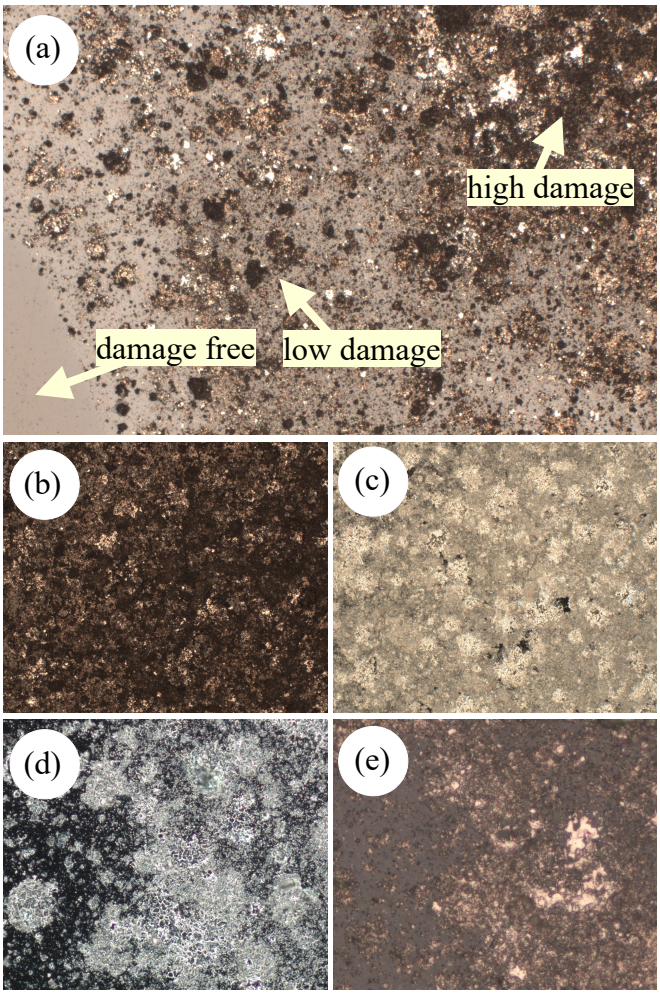

FIG. 9: Detailed microscope images of the polarizer-sided sputter plate. (a) A region that shows the transition from damage free to high damage areas captured with a 5x magnified bright field acquisition (full width corresponds to 3 mm), (b + c) a high damage area as (b) 5x magnified bright field and (c) 5x magnified dark field (full width corresponds to 3 mm respectively), as well as (d + e) a low damage area as (d) 20x magnified dark field (full width corresponds to 0.75 mm) and (e) 50x magnified bright field (full width corresponds to 0.3 mm).

4. Microscope image

Optical microscopy is deployed to capture views on the sputter plate, i.e. color images of the front-side sputter plate are shown in Fig. 9. One notes a abrupt transition from damage free regions to regions with low damage density. Then there is a gradual increase of the damage density toward a region which is heavily damaged.

https://doi.org/10.1017/hpl.2025.12 Published online by Cambridge University Press

[1] T. M. Jeong and J. Lee, Femtosecond petawatt laser, Annalen der Physik 526, 157 (2014)
[2] C. J. Hooker, S. Blake, O. Chekhlov, R. J. Clarke, J. L. Collier, E. J. Divall, K. Ertel, P. S. Foster, S. J. Hawkes, P. Holligan, B. Landowski, B. J. Lester, D. Neely, B. Parry, R. Pattathil, M. Streeter, B. E. Wyborn, Commissioning the Astra Gemini Petawatt Ti:Sapphire Laser System, in CLEO (OSA Technical Digest), paper JThB2 (2008)
[3] T. J. Yu, S. K. Lee, J. H. Sung, J. W. Yoon, T. M. Jeong, J. Lee, Generation of high-contrast, 30 fs, 1.5 PW laser pulses from chirped-pulse amplification Ti:sapphire laser, Opt. Express 20, 10807 (2012)
[4] W. P. Leemans, J. Daniels, A. Deshmukh, A. J. Gonsalves, A. Magana, H. S. Mao, D. E. Mittelberger, K. Nakamura, J. R. Riley, D. Syversrud, Bella laser and operations, in Proc. PAC, 1097–1100 (2013)
[5] J. H. Sung, H. W. Lee, J. Y. Yoo, J. W. Yoon, C. W. Lee, J. M. Yang, Y. J. Son, Y. H. Jang, S. K. Lee, C. H. Nam, 4.2 PW, 20 fs Ti: sapphire laser at 0.1 Hz, Opt. Lett. 42, 2058 (2017)
[6] W. Li, Z. Gan, L. Yu, C. Wang, Y. Liu, Z. Guo, L. Xu, M. Xu, Y. Hang, J. Xu, J. Wang, P. Huang, H. Cao, B. Yao, X. Zhang, L. Chen, Y. Tang, S. Li, X. Liu, S. Li, M. He, D. Yin, X. Liang, Y. Leng, R. Li, Z. Xu, 339 J high-energy Ti: sapphire chirped-pulse amplifier for 10 PW laser facility, Opt. Lett. 43, 5681 (2018)
[7] F. Lureau, G. Matras, O. Chalus, C. Derycke, T. Morbieu, C. Radier, O. Casagrande, S. Laux, S. Ricaud, G. Rey, A. Pellegrina, C. Richard, L. Boudjemaa, C. Simon-Boisson, A. Baleanu, R. Banici, A. Gradinariu, C. Caldararu, B. De Boisdeffre, P. Ghenuche, A. Naziru, G. Kolliopoulos, L. Neagu, R. Dabu, I. Dancus, D. Ursescu, High-energy hybrid femtosecond laser system demonstrating 2×10 PW capability, High Power Laser Sci. Eng. 8, e43 (2020)
[8] C. Danson, D. Hillier, N. Hopps, D. Neely, Petawatt class lasers worldwide, High Power Laser Science and Engineering , Volume 3 , 2015 , e3 (2015)
[9] Y. Wang, S. Wang, A. Rockwood, B. M. Luther, R. Hollinger, A. Curtis, C. Calvi, C. S.. Menoni, J. J. Rocca, 0.85 PW laser operation at 3.3 Hz and high-contrast ultrahigh-intensity λ 400 nm second-harmonic beamline, Opt. Lett. 42, 19, 3828-3831 (2017)
[10] H. Daido, M. Nishiuchi, A. S. Pirozhkov, Review of laser-driven ion sources and their applications, Rep. Prog. Phys. 75 056401 (2012)
[11] M. Borghesi, Ion Acceleration: TNSA and Beyond, Springer Proceedings in Physics 231 (2019)
[12] T. Tajima and V. Malka, Laser plasma accelerators, Plasma Physics and Controlled Fusion 62, 034004 (2012)
[13] P. A. Norreys; M. Santala; E. Clark; M. Zepf; I. Watts; F. N. Beg; K. Krushelnick; M. Tatarakis; A. E. Dangor; X. Fang; P. Graham; T. McCanny; R. P. Singhal; K. W. D. Ledingham; A. Creswell; D. C. W. Sanderson; J. Magill; A. Machacek; J. S. Wark; R. Allott; B. Kennedy; D. Neely, Observation of a highly directional γ-ray beam from ultrashort, ultraintense laser pulse interactions with solids, Phys. Plasmas 6, 2150–2156 (1999)
[14] R. Lichters, J. Meyer-ter-Vehn, A. Pukhov, Short-pulse laser harmonics from oscillating plasma surfaces driven at relativistic intensity, Plasmas 3, 9, 3425 (1996)
[15] P. B. Corkum and F. Krausz, Attosecond science, Nat. Phys. 3, 381 (2007)
[16] F. N. Beg, A. R. Bell, A. E. Dangor, C. N. Danson, A. P. Fews, M. E. Glinsky, B. A. Hammel, P. Lee, P. A. Norreys, M. Tatarakis, A study of picosecond laser–solid interactions up to 1e19 Wcm-2, Phys. Plasmas 4, 2, 447 (1997)
[17] V. Bleko, P. Karataev, A. Konkov, K. Kruchinin, G. Naumenko, A. Potylitsyn, T. Vaughan, Journal of Physics: Conference Series 732, 012006 (2016)
[18] J. Bin, L. Obst-Huebl, J. -H. Mao, K. Nakamura, L. D. Geulig, H. Chang, Q. Ji, L. He, J. De Chant, Z. Kober, A. J. Gonsalves, S. Bulanov, S. E. Celniker, C. B. Schroeder, C. G. R. Geddes, E. Esarey, B. A. Simmons, T. Schenkel, E. A. Blakely, S. Steinke, A. M. Snijders, A new platform for ultra-high dose rate radiobiological research using the BELLA PW laser proton beamline, Scientific Reports 12, 1484 (2022)
[19] N. Xu, M. J. V. Streeter, O. C. Ettlinger, H. Ahmed, S. Astbury, M. Borghesi, N. Bourgeois, C. B. Curry, S. J. D. Dann, N. P. Dover, T. Dzelzainis, V. Istokskaia, M. Gauthier, L. Giuffrida, G. D. Glenn, S. H. Glenzer, R. J. Gray, J. S. Green, G. S. Hicks, C. Hyland, M. King, B. Loughran, D. Margarone, O. McCusker, P. McKenna, C. Parisuaña, P. Parsons, C. Spindloe, D. R. Symes, F. Treffert, C. A. J. Palmer, and Z. Najmudin, Versatile tape-drive target for high-repetition-rate laser-driven proton acceleration, High Power Laser Science and Engineering 11, e23 (2023)
[20] S. J. Haney, K. W. Berger, G. D. Kubiak, P. D. Rockett, J. Hunter, Prototype highspeed tape target transport for a laser plasma soft-x-ray projection lithography source, Appl. Opt. 32(34):6934–6937 (1993)
[21] Y. Jiang, T. Lee, W. Li, G. Ketwaroo, C. G. Rose-Petruck, High-average-power 2kHz laser for generation of ultrashort x-ray pulses, Opt. Lett. 27, 11, 963-965 (2002)
[22] S. Fujioka, H. Nishimura, K. Nishihara, N. Miyanaga, Y. Izawa, K. Mima, Y. Shimada A. Sunahara, Laser production of extreme ultraviolet light source for the next generation lithography application, Plasma and Fusion Research: Review Articles 4, 048 (2009)
[23] M. Roth, T. E. Cowan, M. H. Key, S. P. Hatchett, C. Brown, W. Fountain, J. Johnson, D. M. Pennington, R. A. Snavely, S. C. Wilks, K. Yasuike, H. Ruhl, F. Pegoraro, S. V. Bulanov, E. M. Campbell, M. D. Perry, H. Powell, Fast Ignition by Intense Laser-Accelerated Proton Beams, Physical Review Letters 86, 3, 436-439 (2001)
[24] K. W. D. Ledingham, P. McKenna, T. McCanny, S. Shimizu, J. M. Yang, L. Robson, J. Zweit, J. M. Gillies, J. Bailey, G. N. Chimon, R. J. Clarke, D. Neely, P. A. Norreys, J. L. Collier, R. P. Singhal, M. S. Wei, S. P. D. Mangles, P. Nilson, K. Krushelnick, M. Zepf, High power laser production of short-lived isotopes for positron emission tomography, Journal of Physics D: Applied Physics 37 2341 (2004)
[25] J. E. Andrew and K. A.Wallace , Characterisation of contaminant plumes arising from laser-solid target interactions, Proc. SPIE 7842, Laser-Induced Damage in Optical Materials: 2010, 78420R (2010)

https://doi.org/10.1017/hpl.2025.12 Published online by Cambridge University Press

[26] M. Ehret, J. I. Apiñaniz, J. L. Henares, R. Lera, D. de Luis, J. A. Pérez-Hernández, L. Volpe, G. Gatti, Ablation holes in tape targets induced by ultra-intense laser pulses, NIMB 541, 165-168 (2023)

[27] N. Booth, S. Astbury, E. Bryce, R. J. Clarke, C. D. Gregory, J. S. Green, D. Haddock, R. I. Heathcote, C. Spindloe, Debris studies for high-repetition rate and high-power laser experiments at the Central Laser Facility, Proc. SPIE 10763, Radiation Detectors in Medicine, Industry, and National Security XIX, 107630S (2018)

[28] T. Ando, S. Fujioka, Y. Shimada, T. Birou, S. Maeda, Y. Yasuda, K. Nagai, T. Norimatsu, H. Nishimura, K. Nishihara et al., Jpn. J. Appl. Phys. 47, 293 (2008)

[29] S. Amano, Y. Inaoka, H. Hiraishi, S. Miyamoto, T. Mochizuki, Laser-plasma debris from a rotating cryogenic–solid-Xe target, Review of Scientific Instruments 81, 023104 (2010)

[30] J. Andrew, J.-M. Chevalier, D. Egan, A. Geille, J.-P. Jadaud, J.-H. Quessada, D. Raffestin, M. Rubery, P. Treadwell, L. Videau, Dedicated contamination experiments in the Orion laser target chamber, Proc. SPIE 9632, Laser-Induced Damage in Optical Materials: 2015, 96320E (2015)

[31] D. Doria, M. O. Cernaianu, P. Ghenuche, D. Stutman, K. A. Tanaka, C. Ticos, C. A. Ur, Overview of ELI-NP status and laser commissioning experiments with 1 PW and 10 PW class-lasers, JINST 15 C09053 (2020)

[32] C.N. Danson, P.A. Brummitt, R.J. Clarke, J.L. Collier, B. Fell, A.J. Frackiewicz, S. Hancock, S. Hawkes, C. Hernandez-Gomez, P. Holligan, M.H.R. Hutchinson, A. Kidd, W.J. Lester, I.O. Musgrave, D. Neely, D.R. Neville, P.A. Norreys, D.A. Pepler, C.J. Reason, W. Shaikh, T.B. Winstone, R.W.W. Wyatt and B.E. Wyborn, Vulcan Petawatt—an ultra-high-intensity interaction facility, Nuclear Fusion, 44, S239 (2004)

[33] J. Bromage, S.-W. Bahk, D. Irwin, J. Kwiatkowski, A. Pruyne, M. Millecchia, M. Moore, and J. D. Zuegel, A focal-spot diagnostic for on-shot characterization of high-energy petawatt lasers, Optics Express, 16, 16561-16572 (2008)

[34] Alexander S. Pirozhkov, Yuji Fukuda, Mamiko Nishiuchi, Hiromitsu Kiriyama, Akito Sagisaka, Koichi Ogura, Michiaki Mori, Maki Kishimoto, Hironao Sakaki, Nicholas P. Dover, Kotaro Kondo, Nobuhiko Nakanii, Kai Huang, Masato Kanasaki, Kiminori Kondo, and Masaki Kando, Approaching the diffraction-limited, bandwidth-limited Petawatt, Optics Express, 25, 20486-20501 (2017)

[35] D. Haddock, S. Astbury, I.-M. Vladisavlevici, M. Ehret, Ph. W. Bradford, Optical profilometry of the surface of debris catchers used in laser-plasma experiments at ELI-NP, Central Laser Facility & Centro de Láseres Pulsados, Zenodo 14094980 (2024) https://doi.org/10.5281/zenodo.14094980

[36] X. Chen, J. Zhao, S. Xu, Z. Peng, L. Ma, Y. Gao, S. Chen, Z. Liu, S. Xu, Z. Pan, Y. g, T. Song, T. Xu, X. Yan, W. Ma, A design of debris mitigation system for high-repetition-rate petawatt laser experiments, Nuclear Instruments and Methods in Physics Research Section A: Accelerators, Spectrometers, Detectors and Associated Equipment 1060, 169073 (2024)

[37] T. Sano, H. Yamada, T. Nakayama, I. Miyamoto, Experimental investigation of laser induced forward transfer process of metal thin films, Applied Surface Science 186, 1–4, 221-226 (2002)

[38] P. Papakonstantinou, N. A. Vainos, C. Fotakis, Microfabrication by UV femtosecond laser ablation of Pt, Cr and indium oxide thin films, Applied Surface Science 151, 3–4, 159-170 (1999)

[39] G. Hennig, T. Baldermann, C. Nussbaum, M. Rossier, A. Brockelt, L. Schuler, G. Hochstein, Lasersonic LIFT Process for large area digital printing, Journal of Laser Micro/Nanoengineering 7, 3 (2012)

[40] M. Rycenga, C. M. Cobley, J. Zeng, W. Li, C. H. Moran, Q. Zhang, D. Qin, Y. Xia, Chem Rev. 111(6): 3669–3712 (2011)

[41] R. Kitamura, L. Pilon, and M. Jonasz, Optical constants of silica glass from extreme ultraviolet to far infrared at near room temperature, Appl. Opt. 46, 8118-8133 (2007)

[42] I. H. Malitson, Interspecimen comparison of the refractive index of fused silica, J. Opt. Soc. Am. 55, 1205-1208 (1965)

[43] R. Swanepoel, Determination of the thickness and optical constants of amorphous silicon, J. Phys. E: Sci. Instrum. 16 1214 (1983)

[44] J. M. Lárraga-Gutiérrez, O. A. García-Garduño, C. Treviño-Palacios, J. A. Herrera-González, Evaluation of a LED-based flatbed document scanner for radiochromic film dosimetry in transmission mode, Physica Medica 47, 86-91 (2018)

[45] P. B. Johnson and R. W. Christy, Optical constants of transition metals: Ti, V, Cr, Mn, Fe, Co, Ni, and Pd, Phys. Rev. B 9, 5056-5070 (1974)

[46] A. Axelevitch, B. Gorenstein, G. Golan, Investigation of optical transmission in thin metal films, Physics Procedia 32, 1-13 (2012)

https://doi.org/10.1017/hpl.2025.12 Published online by Cambridge University Press